nature biomedical engineering

ARTICLES

https://doi.org/10.1038/s41551-021-00817-7

Check for updates

Chronic electrical stimulation of peripheral nerves via deep-red light transduced by an implanted organic photocapacitor

Malin Silverå Ejneby[1,2,8], Marie Jakešová[1,3,8], Jose J. Ferrero[4,8], Ludovico Migliaccio[1,2,3,8], Ihor Sahalianov[1], Zifang Zhao[5], Magnus Berggren[1], Dion Khodagholy[5], Vedran Đerek[1,2,6] ✉, Jennifer N. Gelinas[4,7] ✉ and Eric Daniel Głowacki[1,2,3] ✉

Implantable devices for the wireless modulation of neural tissue need to be designed for reliability, safety and reduced invasiveness. Here we report chronic electrical stimulation of the sciatic nerve in rats by an implanted organic electrolytic photocapacitor that transduces deep-red light into electrical signals. The photocapacitor relies on commercially available semiconducting non-toxic pigments and is integrated in a conformable 0.1-mm³ thin-film cuff. In freely moving rats, fixation of the cuff around the sciatic nerve, 10 mm below the surface of the skin, allowed stimulation (via 50–1,000-μs pulses of deep-red light at wavelengths of 638 nm or 660 nm) of the nerve for over 100 days. The robustness, biocompatibility, low volume and high-performance characteristics of organic electrolytic photocapacitors may facilitate the wireless chronic stimulation of peripheral nerves.

Implantable neural interfaces are at the heart of bioelectronic medicine[1–3]. Direct electrical actuation of the nervous system is used clinically in deep brain stimulation[4], prosthetic retinal implants[5], vagus-nerve stimulation for the treatment of epilepsy[6] and other disorders[7,8], as well as in numerous other applications, and the list of emerging technologies at a preclinical phase is constantly growing[9,10]. However, several fundamental engineering hurdles need to be overcome to facilitate widespread implementation of bioelectronic devices and to ensure optimal clinical outcomes[11,12]. A key challenge is to improve the long-term powering and miniaturization of implantable devices, motivating the exploration of methods to wirelessly actuate and control implants from outside the body. The most common approaches involve radiofrequency (RF) power transmission or electromagnetic induction[13]. Although these technologies are being developed for clinical use[11,14–16], the RF approach imposes size and shape constraints for the transmitting and receiving components. The volumes of the receivers (implanted inside the body) presently range from 30 to 600 mm³ (ref. [17]), as they include antennas for RF transmission, electrodes for nerve stimulation and device packaging for the protection of rigid Si-based electronics from body fluids. Efficient RF coupling and tissue heating are also factors that limit clinical translation[17]. An alternative emerging approach leverages acoustic waves at ultrasound frequencies. Ultrasonic energy can be used to stimulate nervous tissue directly[18] or can be absorbed by piezoelectric transducers to power devices[19]. Although promising, because of acoustic impedance-matching requirements, the ultrasound transmitter must be in intimate contact with the skin, and penetration through layers of different tissues can be a limitation of such ultrasound technologies. Overall, there is a strong demand for fully implantable systems that require less anatomical space than the aforementioned approaches, and that are minimally invasive, remotely powered and easy to use.

Optical power transfer has been proposed as an alternative approach[20,21]. We hypothesized that tissue-penetrating deep-red light (620–800 nm) could effectively control and power implants wirelessly, without requiring rigid or bulky implanted components. Four main features support this idea. First, deep-red wavelengths occupy the tissue-transparency window of the electromagnetic spectrum, in which the absorbance spectra of biopigments in the body and of water have local minima. As a consequence, light in the 620–800 nm region has relatively good penetration depth in skin, muscle and fat tissue[22]. Second, light-emitting diode (LED) technologies are well-established and mature. High-brightness and efficient LED light sources are reliable and commercially available in large variety and at low cost. Third, light-based technologies are widely accepted in medical practice, in both therapeutic and imaging applications. Finally, devices relying on optical power transfer can be made easily at the submillimetre scale (volume of <1 mm³) because of the availability of relatively efficient and easily processable thin-film photovoltaic materials. The use of deep-red light could therefore overcome the challenge of making small-scale devices that can be actuated and controlled wirelessly from outside the body.

The combination of an optoelectronic transducer implant and deep-red light has been explored less than other power-transfer methods, although several promising examples do exist[20]. Recent efforts have demonstrated light-powered and rechargeable pacemakers[23,24], while pioneering work on inorganic photovoltaic stimulators has shown acute in vivo efficacy for spinal-cord stimulation, relying on power transfer through ~3 mm of tissue[25]. Recently,

[1]Laboratory of Organic Electronics, Campus Norrköping, Linköping University, Norrköping, Sweden. [2]Wallenberg Centre for Molecular Medicine, Linköping University, Linköping, Sweden. [3]Central European Institute of Technology, Brno University of Technology, Brno, Czech Republic. [4]Institute for Genomic Medicine, Columbia University Medical Center, New York, NY, USA. [5]Department of Electrical Engineering, Columbia University, New York, NY, USA. [6]Department of Physics, Faculty of Science, University of Zagreb, Zagreb, Croatia. [7]Department of Neurology, Columbia University Medical Center, New York, NY, USA. [8]These authors contributed equally: Malin Silverå Ejneby, Marie Jakešová, Jose J. Ferrero, Ludovico Migliaccio. ✉e-mail: vdjerek@phy.hr; jng2146@cumc.columbia.edu; eric.daniel.glowacki@ceitec.vutbr.cz

flexible on-skin LED arrays have been shown to accomplish efficient optical power transfer to implanted photovoltaic arrays based on GaAs, and such arrays were shown to recharge the batteries of an implanted stimulator[21]. A variety of approaches in basic and biomedical research use light to mediate neurostimulation because of its non-invasiveness and versatility[26–28]. Optogenetics endows cells with light responsiveness[29], but the necessity of genetic manipulation to accomplish this is not always facile or desirable for many applications and remains a controversial proposition for clinical translation. Moreover, few opsins are available with light sensitivity in the red part of the spectrum[30]. Over the past decade, these observations have spurred exploration of other ways to use light to interface with the nervous system. Photothermal heating with light can be used directly to trigger a thermocapacitive effect, stimulating neurons in vitro[31]. To better control the specificity and localization of this approach, light-absorbing nanoparticles or microparticles can be used as photothermal mediators[32]. Both inorganic[33] (primarily Si)[34] and molecular[35] or polymeric[36] semiconductors can be used as light absorbers for various in vitro stimulation demonstrations. Nanoscale Si biointerfaces can be tuned to provide highly localized photocurrent stimulation in single cells[28]. Few of these concepts have proven scalable or reliable for in vivo settings, and chronic deployment remains elusive. So far, photovoltaic neurostimulation has been developed for retinal protheses, based on arrays of Si[37] or organic semiconductors[38]. Highly optimized Si diode-based technologies for retinal stimulation[39,40] have advanced to clinical trials. Delivery of light is straightforward for intraocular applications, but getting sufficient light to devices implanted below the skin and other tissues is not so easy. We propose the use of organic semiconductors as the active optoelectronic component to facilitate light-mediated neurostimulation for such applications[41] because of their high absorbance coefficient (10–1,000 times greater than Si), mechanical flexibility and biocompatibility[42]. These can enable ultrathin and minimally invasive form factors that are inaccessible in traditional inorganic materials.

Our biointerfacial devices use commercially available organic pigments[35,43] that belong to the category of safe and non-toxic colourants approved for a wide range of consumer products such as food colourants and cosmetics[44]. Their non-toxicity originates from their non-bioavailability, which in turn results from their complete insolubility and the formation of stable crystals. The specific pigments that we used, phthalocyanine and rylene diimide pigments, have a low-energy molecular structure based on aromatic carbon–nitrogen heterocycles. These intrinsically robust molecular motifs are further stabilized by strong intermolecular interactions mediated by π–π stacking and hydrogen bonding. These forces lead to the formation of organic pigment nanocrystals that have, aside from favourable electronic properties, outstanding stability in aqueous environments. For these reasons, we postulate that this class of organic material may be sufficiently resistant to degradation to enable stable in vivo interface devices. These pigment materials form the basis of our recently developed organic electrolytic photocapacitor (OEPC)[45]. This device employs a nanocrystalline donor–acceptor p–n junction that acts as the charge-generating element and primary stimulation electrode, which is surrounded by a concentric return electrode. The stimulation efficacy of this minimalistic device architecture has been validated for cultured neurons and in explanted retinal tissues[45]. More recently, its capacitive charging behaviour was characterized at the single-cell level, accompanied by the direct electrophysiological measurement of the device's impact on voltage-gated ion channels[46,47]. These in vitro demonstrations were based on rigid OEPCs. In this Article we integrate the OEPC into an ultrathin flexible architecture suitable for chronic in vivo implantation. The photoelectrical charging behaviour of the OEPC stimulation devices effectively activated the rat sciatic nerve in vivo, and enabled precise control of the stimulation by varying the light intensity and pulse duration. We fabricated the OEPC into a self-locking ultrathin cuff that was simple to surgically place and immobilize inside an animal that was freely moving over a period of months. Deep-red light delivered through the skin surface to the implanted OEPC evoked compound muscle action potentials (CMAPs)[48] via sciatic-nerve stimulation at an operation depth of ~10 mm. The device implantation did not impede physiological motor behaviour, and the devices maintained their operation for up to three months after implantation. With a total volume of 0.1 mm^3, these OEPCs are the lowest-volume wireless peripheral nerve interface reported so far[17]. The results suggest that OEPCs provide a viable approach to achieving chronic in vivo neurostimulation and have potential for clinical translation.

Results

Design and fabrication of flexible OEPC nerve stimulators. Our approach to wireless neurostimulation leverages organic molecular thin films to efficiently transduce light impulses into electrolytic currents that modulate the activity of excitable cells. As in our in vitro studies leading up to the present work[45,46], we rely on the phthalocyanine (H_2Pc, p-type)/*N*,*N*′-dimethyl perylenetetracarboxylic bisimide/(PTCDI, n-type) heterojunction to create OEPCs (Fig. 1a). The bilayer is deposited by thermal vacuum evaporation to form a densely packed film of nanocrystals (Fig. 1b). This p–n junction combination has high reliability and stability in aqueous environments. To transform the OEPC into an implantable device capable of efficiently delivering a stimulation current, we integrated it into a ribbon-like structure that can conform around the nerve. We used thin (5 μm) parylene C, a well-established biocompatible polymer, as a substrate material[49]. The first design challenge we faced was producing a semi-transparent conducting back electrode layer on the substrate. A key materials selection criterion is the

Fig. 1 | OEPCs wirelessly stimulate the sciatic nerve in vivo. a, Molecular structures of the active components in the p–n semiconducting layer. Phthalocyanine (H_2Pc) functions as the light-absorbing and electron-donating p-type layer. PTCDI acts as the electron-accepting n-type layer and forms an electrolytic contact with the surrounding electrolyte. **b**, The sequentially evaporated p–n bilayer (30 + 30 nm) forms a compact thin film featuring a distinctive nanocrystalline morphology that is apparent in scanning electron microscopy. Scale bar, 200 nm. **c**, Diagram of the OEPC device and its operating principle. The p–n bilayer is processed on top of a semi-transparent gold film (10 nm), which acts as the return (+) electrolytic contact. Light in the deep-red region (638 or 660 nm) is used for excitation of the p-type layer. Photogenerated electrons travel through the n layer to accumulate at the electrolyte interface, forming an electrolytic double layer. Concurrently, holes are driven from the p layer into the underlying gold, forming an oppositely charged double layer. During charging of the device (beginning of the light pulse) and discharging (end of the light pulse), ionic displacement currents (transient ionic current, I_{ionic}) flow around the device and thus through the surrounding tissue. This produces biphasic stimulation pulses. The inset shows how the OEPC, understood simply as an illuminated photodiode, couples to a nerve with a quasi-tripolar arrangement. **d**, Schematic of the in vivo implanted OEPC photostimulation experiments performed in this study. Scale bar, 1 cm. The inset details how a CIP cuff is placed around the nerve, with the configuration of the primary p–n photoelectrode (−) with the surrounding (+) return electrode. **e**, Following implantation, deep-red light penetrates through skin, fat and muscle tissues to reach the OEPC, located at a depth *z* of ~10 mm. **f**, Numerical calculation of the penetration of a stimulating red light beam through simulated animal tissue layers, showing the effectiveness of a 638-nm light beam of radius *r* from the beam center 0 in accessing the implanted OEPC. The dotted white line represents the cross-sectional region with 50 mW cm^{-2} of intensity.

semitransparency of this underlying conductor, such that light can reach the absorbing p–n semiconductor layer. We used thin thermally evaporated Au (thickness of 10 nm) because of its excellent conductivity, good transparency and mechanical flexibility[45]. In the OEPC architecture, the back conductor functions as a return electrode, completing the current path generated by the p–n junction. The p–n junction, under illumination, will produce an electrolytic double layer as electrons accumulate at the n-type material/electrolyte interface. Meanwhile, holes are driven into the underlying metallic conductor, creating an oppositely charged double layer around the p–n pixel, thus giving rise to ionic displacement currents around the device (I_{ionic}, Fig. 1c). From the point of view of an underlying nerve, this device architecture produces a tripolar-type stimulating electrode arrangement (Fig. 1c, inset)[12]. These materials were integrated to ultimately fabricate chronically implantable photocapacitors (CIPs) for testing in an animal model. We placed these devices on the rat sciatic nerve intra-operatively and subsequently implanted them for long-term in vivo evaluation (Fig. 1d). During

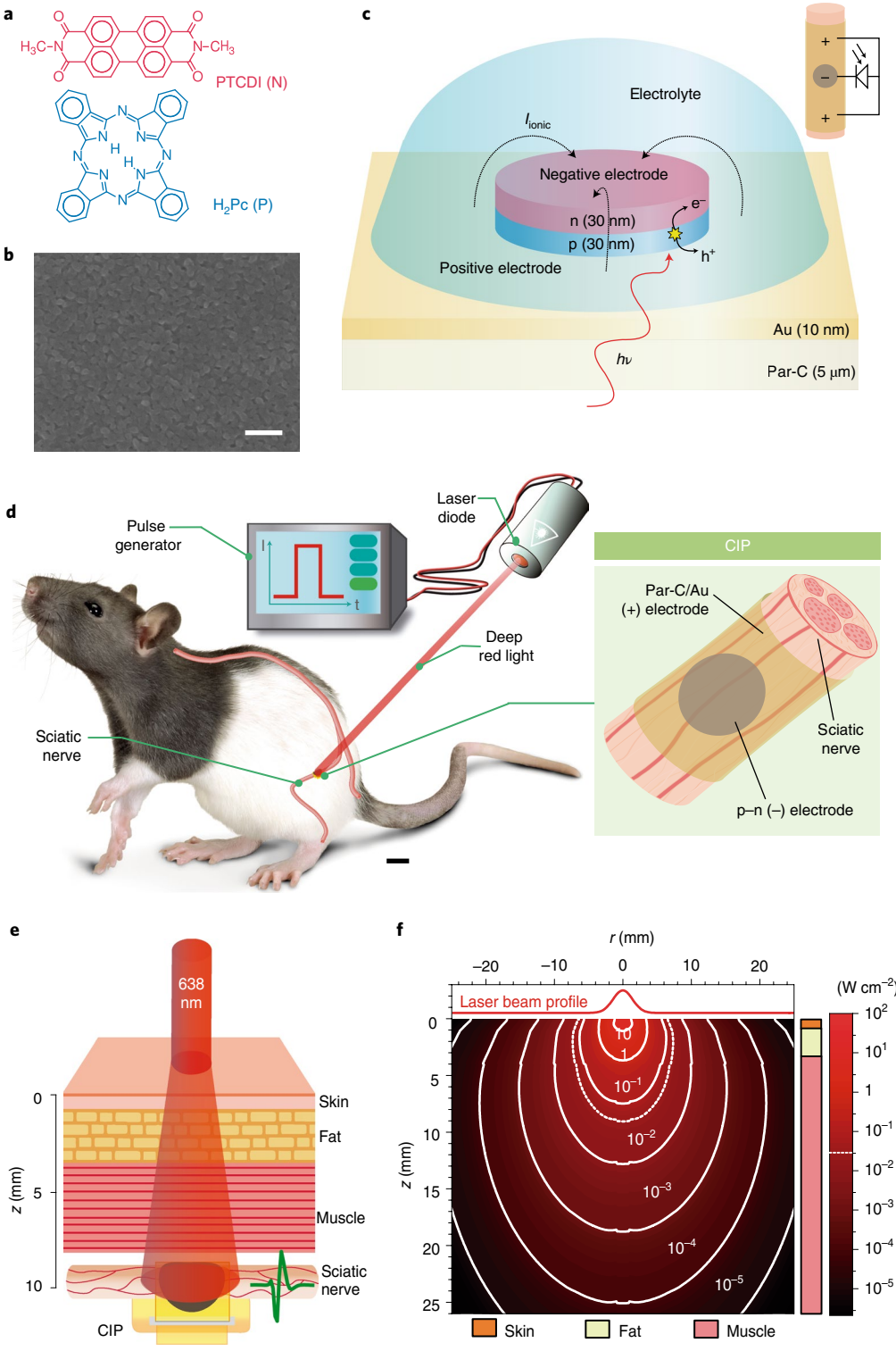

chronic photostimulation, 638-nm light impulses would need to be beamed through ~10 mm of tissue to drive the CIP (Fig. 1e). We first sought to investigate the feasibility of this approach to find whether light can be transmitted efficiently and safely to reach a device located below the surface of the skin. Light propagation through different tissues has been studied in detail[22]. We applied established numerical Monte Carlo (MC) methods[50,51] and used known optical constants for rat tissue[52] to determine that a conventional 700-mW laser diode at 638 nm will deliver light intensities in the range of tens of milliwatts per square centimetre at a depth of 1 cm (Fig. 1f). It is also critical to consider the light power safety. To first order, in all experiments in this work we set a limit on the light dose to a maximum of ten times below the accepted laser safety standards for skin exposure according to the American National Safety Standard for the use of Lasers[53], according to which the maximum permissible exposure for skin is 195 mJ cm^{-2}. A 700-mW laser diode, on an area of 4 mm^2 and with a 1-ms pulse, yields 17.5 mJ cm^{-2}. To understand the magnitude of photothermal effects, we combined our MC calculations with finite-element methods to construct a heat-dissipation model for light impinging on live rat tissue (Supplementary Appendix 1). From this model it emerged that if relatively high light powers (~1 W) are delivered over relatively short periods of time (≤1 ms), the total dissipated heat is negligibly low, causing a temperature increase on the order of a thousandth of a degree. Heat is transferred differently in the various tissue layers, with the largest relative change appearing at the surface of the skin. The largest photothermal change is 0.005 °C with the longest illumination time of 1 ms. Furthermore, we find no evidence for photothermal effects on neural tissue when operating these devices in vivo (Fig. 3).

Photoelectrical characterization. Although stimulation electrode benchmarking methods are well established[54,55], determining parameters relevant for an electrically floating photoelectrode device requires special consideration. A common figure of merit for a neurostimulation electrode is the electrolytic charge density that the electrode can inject, or the charge density per phase[54]. To measure this parameter in OEPCs, we devised the electrophotoresponse (EPR) method[46] (Fig. 2a). In EPR, the photovoltage or photocurrent is registered by contacting the back electrode (Au) with a probe and measuring versus an ideally non-polarizable electrode (Ag/AgCl) immersed in electrolyte. This electrolyte is confined to the top of the p–n semiconductor region. The device is illuminated by light pulses from the bottom, through the semi-transparent gold film, thus mimicking the anticipated configuration during in vivo neurostimulation. The photovoltage to which the p–n/electrolyte junction charges can be measured using an oscilloscope. Photocurrent is quantified in the same arrangement using a current amplifier. During a 638- or 660-nm light pulse, the OEPC charges to ~300–320 mV and the capacitive displacement currents under the same conditions peak at ~2 mA cm^{-2} (Fig. 2b). The photovoltage in this configuration represents the thermodynamics of the p–n junction band-edge in contact with the electrolyte. Most relevant to neurostimulation applications, the photocurrent measurement quantifies the charge that can be injected as a function of light intensity and pulse length. The dynamics are rapid, with the maximum charging current peaking at 20 µs. In the context of OEPC devices, the charge density can be modulated with the light intensity and light pulse length. We plot the charge density per phase as a function of light intensity in Fig. 2c and as a function of light pulse duration, from 50 µs to 1 ms, in Fig. 2d. The 638-nm wavelength was found to have slightly better photocharging efficiency than with 660 nm. This finding corresponds to the absorption spectrum of the H_2Pc p-type absorber layer[45]. Importantly, both wavelengths are typical in readily available LED illuminators.

Although the EPR measurement allows quantification of the photocharge density that the OEPC device can generate, it does not faithfully reflect the final operating conditions of an OEPC stimulator. In vivo, the OEPC device is electrically floating. The organic p–n pixel forms an electrolytic closed circuit with the back electrode[45,56]. The displacement current that flows around the device during photocharging and discharging generates transient potentials in the solution that affect the electrophysiology of nearby cells, as established in our earlier in vitro studies[46,47]. To visualize this effect, we measure the transient potential (V_T) above the p–n pixel in the electrolyte (Fig. 2e). V_T was registered between a recording microelectrode positioned 1 mm above the centre of the p–n pixel versus a distant reference electrode. Consistent with the p–n polarity of the OEPC, illumination resulted in a cathodic transient voltage peak followed by an anodic transient when the light was turned off and electronic charge carriers recombined (Fig. 2f, inset). This voltage transient corresponds temporally to the electrical perturbation that adjacent axon bodies will experience. It mimics a charge-balanced biphasic stimulation protocol, which is typically used to avoid tissue and electrode damage during neurostimulation[57,58]. The actual transmembrane potential induced will vary based on the position and distance from the stimulating electrode[46,59]. The magnitude of V_T was directly proportional to the size of the p–n pixel, ranging from ~8 mV for a 1-mm-diameter p–n pixel to 30–40 mV for a 3-mm-diameter pixel (Fig. 2f). Taken together, these results demonstrate the operating mechanism and parameters for OEPC-mediated neural stimulation and highlight the importance of p–n pixel size as a key parameter governing the effectiveness of neuromodulation.

Acute validation of light-induced nerve stimulation. To test the efficacy of in vivo neuromodulation using OEPC devices, we used the well-established rat sciatic nerve model[12,16]. To determine the effectiveness of OEPC-mediated nerve stimulation, microwires capable of measuring evoked CMAPs were placed in the biceps femoris (Fig. 3a) and plantar muscle (Supplementary Fig. 1) groups of five rats. OEPC devices integrated into parylene C ribbons were wrapped around the nerve with the p–n pixel immediately adjacent to the epineurium. The ribbon was not fixed in any way other than simple adhesion of the loose plastic ends to each other via capillary interactions in the presence of water. Intra-operatively, OEPC ribbons with differently sized p–n pixels (diameters of 1 mm, 1.4 mm and 3 mm, denoted henceforth as three device sizes, S, M and L) were illuminated using an LED (660 nm) with a collimator lens that was placed above the exposed nerve (Fig. 3b). OEPCs were consistently placed such that the p–n pixel pointed in the dorsocaudal direction relative to the rat's body. To ensure that any recorded CMAPs were the result of light-mediated photovoltaic stimulation, we conducted experiments with two types of sham device: bare parylene C covered with Au and a device with a photothermal absorber layer, denoted 'thermal control' (TC in Fig. 3c). Illumination of the Au sham device did not yield any response or artefact (Fig. 3d and Supplementary Fig. 1b). This indicated that light impulses alone were not eliciting any stimulation. To evaluate the possibility of photothermal heating, however, it was necessary to add a layer that would absorb light and locally generate heat. For this purpose we deposited thin films of indigo pigment, which has an optical absorption closely mimicking that of the active p–n layer. Indigo dissipates 99%+ of absorbed light as heat[60]. We found that these photothermal control samples also produced no electrophysiological response (Fig. 3d). This allowed us to rule out photothermal stimulation effects. By contrast, illumination of OEPC devices did reproducibly stimulate the sciatic nerve, as demonstrated by visually observable twitching in sciatic-innervated muscles and recorded CMAPs (Fig. 3e shows CMAPs in response to 1-ms illumination pulses at 9.4 mW mm^{-2}) (Supplementary Fig. 1c and Supplementary Video 1). Increasing size of the p–n pixel strongly correlated with higher stimulation, as measured by a larger amplitude of both the observable movement and the average CMAP waveform (Fig. 3e

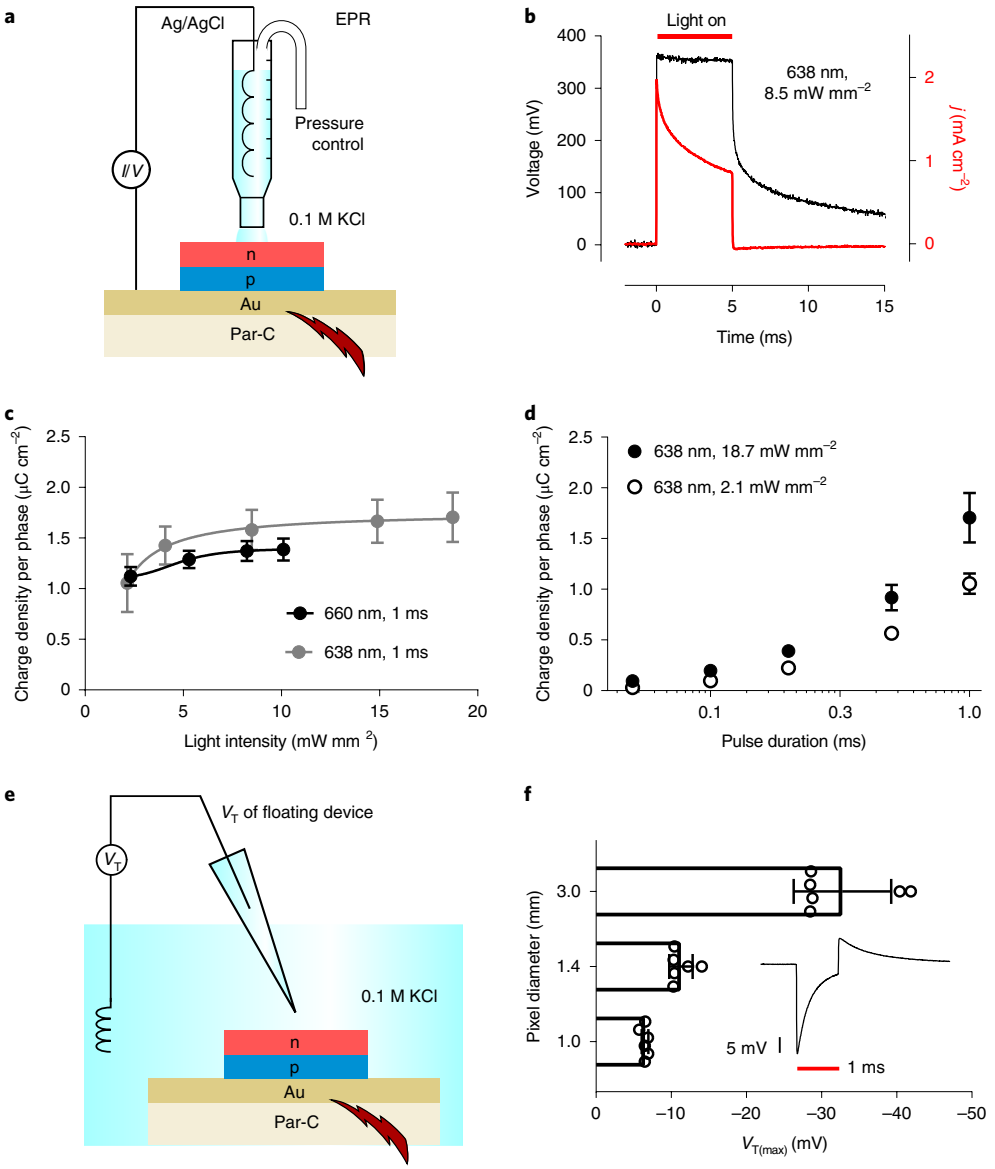

Fig. 2 | Photostimulated OEPC devices deliver rapid localized electrolytic pulses. a, Schematic of the EPR closed-circuit measurement, in which the photovoltage or photocurrent is measured between the bottom metal contact and an electrolytic contact. This method probes photogenerated charge injection across the p–n/electrolyte junction, and the photovoltage reflects the energy levels of the metal/p–n/electrolyte stack. **b**, Photovoltage (black) and photocurrent (red) registered by EPR using excitation with a 638-nm laser diode. **c**, Charge density per phase as a function of light pulse intensity for 1-ms light pulses of either 638- or 660-nm light ($n = 8$, data presented as mean ± s.d.). **d**, Charge density per phase as a function of light pulse duration ($n = 8$, data presented as mean ± s.d.). **e**, The transient voltage, V_T, probes the voltage perturbation generated in the electrolyte when displacement currents flow from the anode (Au) to the cathode (p–n). V_T is registered between a point above the centre of the p–n pixel and a distant Ag/AgCl reference. This method reflects the actual electrical perturbation nerve fibres would experience from the OEPC stimulator. **f**, Inset: V_T during a 1-ms light pulse, showing the clear biphasic current behaviour. All pixels give the same trace qualitatively; only the magnitude of the voltage varies with pixel diameter. The bar graph plots the average cathodic maximum V_T as a function of p–n pixel diameter for 638-nm light at an intensity of 17.5 mW mm^{-2} ($n = 3$ devices for each size, each measured two separate times, data shown ±s.d.).

and Supplementary Fig. 1c), concurring with the predictions of V_T measurements (Fig. 2f). The elicited CMAPs were also highly consistent in both amplitude and latency after repetitive light stimulation (Fig. 3f and Supplementary Fig. 1d; 25 light pulses with 3 s between). Taken together, these results demonstrate the ability of the OEPC to transduce light impulses to electrical potentials that are capable of consistently and repetitively stimulating the sciatic nerve, with response magnitude dependent on p–n pixel size.

In vivo neurostimulation often requires precise control of response timing and amplitude. Using M- and L-sized OEPC devices, we determined the relationship between light intensity and light pulse duration with CMAP responses (Fig. 3g–i and Supplementary Fig. 1e–h). CMAP responses were quantified using the amplitude of the M-wave. The H-wave was detected for a subset of stimulations, namely those with a relatively low charge dose, close to the threshold for visible movement (Supplementary Fig. 1f). For size-M devices, light intensities in the range of 4–10 mW mm^{-2} evoked robust CMAP responses and visible movements in the leg and paw (Fig. 3g,h and Supplementary Fig. 1e,g), and light-pulse durations between 200 and 500 μs were needed to reach a threshold

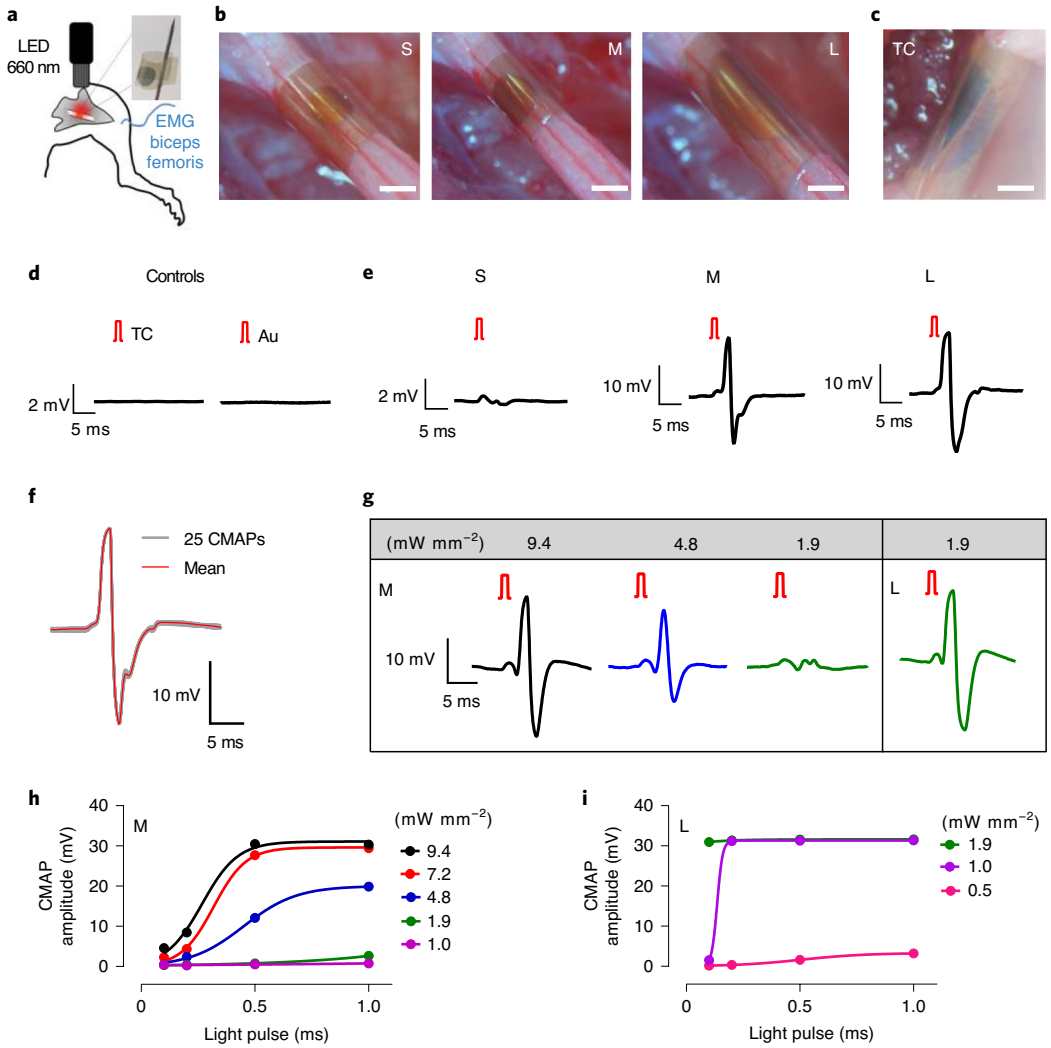

Fig. 3 | Acute sciatic nerve photostimulation is precisely controlled by varying OEPC device size, light intensity and stimulation pulse length. a, Schematic of the sciatic nerve stimulation experiment design for acute conditions. The inset photograph shows a free-standing device before implantation. EMG, electromyography. **b**, Photographs of S, M and L devices wrapped around the sciatic nerve. Scale bars, 1 mm. **c**, An L-sized thermal control (TC) sham, consisting of a pixel of indigo, a pigment that efficiently heats up but does not generate charge. **d**, Illumination of sham devices (only Au on parylene C (Au) or the indigo TC) gives no response or artefact (1-ms light pulses, 9.4 mW mm^{-2} of irradiation). **e**, Averaged evoked CMAPs in the biceps femoris (rat 1) during stimulation by 25 repetitive light pulses (1-ms pulses, 9.4 mW mm^{-2} irradiation, 3 s between) for different-sized OEPC devices. **f**, Highly reproducible repeated stimulation can be shown when 25 CMAPs are plotted on top of each other (in grey) after repetitive stimulation of the biceps femoris with an M-sized OEPC device (rat 1, 1-ms light pulses, 9.4 mW mm^{-2} irradiation, 3 s between). The averaged response is shown in red. **g**, Examples of CMAPs evoked at different light intensities with 1-ms pulses on M- and L-sized OEPC devices (rat 2). **h**, Average biceps femoris CMAP amplitudes versus light-pulse length, at different light intensities, with an M-sized OEPC device (25 pulses, 3 s between, for each condition). **i**, Average biceps femoris CMAP amplitudes versus light-pulse length, at different light intensities, with an L-sized OEPC device (25 pulses, 3 s between, for each condition). The CMAP amplitude saturates at lower intensities and pulse times for the L device as compared with the M device.

of visible movement. With the L-sized OEPC device, the light intensity and light-pulse duration could be reduced substantially (Fig. 3g,i and Supplementary Fig. 1e,h). For example, at 1 mW mm^{-2}, using 1-ms light pulses, the CMAP response is already saturated for both muscles (Fig. 3i and Supplementary Fig. 1h). Shorter light pulses (100 µs) could thus be used to reach a threshold of visible movement. Accordingly, the interplay of light intensity, light-pulse duration and p–n pixel size can be used to produce a given level of OEPC-mediated neurostimulation.

CIP development and implementation. Following on from acute nerve stimulation experiments, we aimed to engineer the OEPC for chronic implantation by developing a more chemically and mechanically stable interface with the nerve. The OEPC relies on an ultrathin Au semi-transparent conductive layer on parylene C as the return (+) electrode. However, we found that this Au layer loses conductivity and delaminates when stored in chloride-containing electrolytes for more than two weeks. This probably precludes its in vivo longer-term use. To stabilize the thin Au, we deposited a 30-nm-thick encapsulating layer of indium tin oxide (ITO), which has excellent adhesion with Au[61]. ITO has a wide electrochemical passivity window[62], is biocompatible[63,64] and does not compromise transparency or conductivity. In the range of potentials and conditions we use in our work, Au/ITO bilayers had suitable stability. Furthermore, the ITO layer enabled convenient new micropatterning approaches based on parylene peel-off lithography[65], serving as an effective etch-stop for

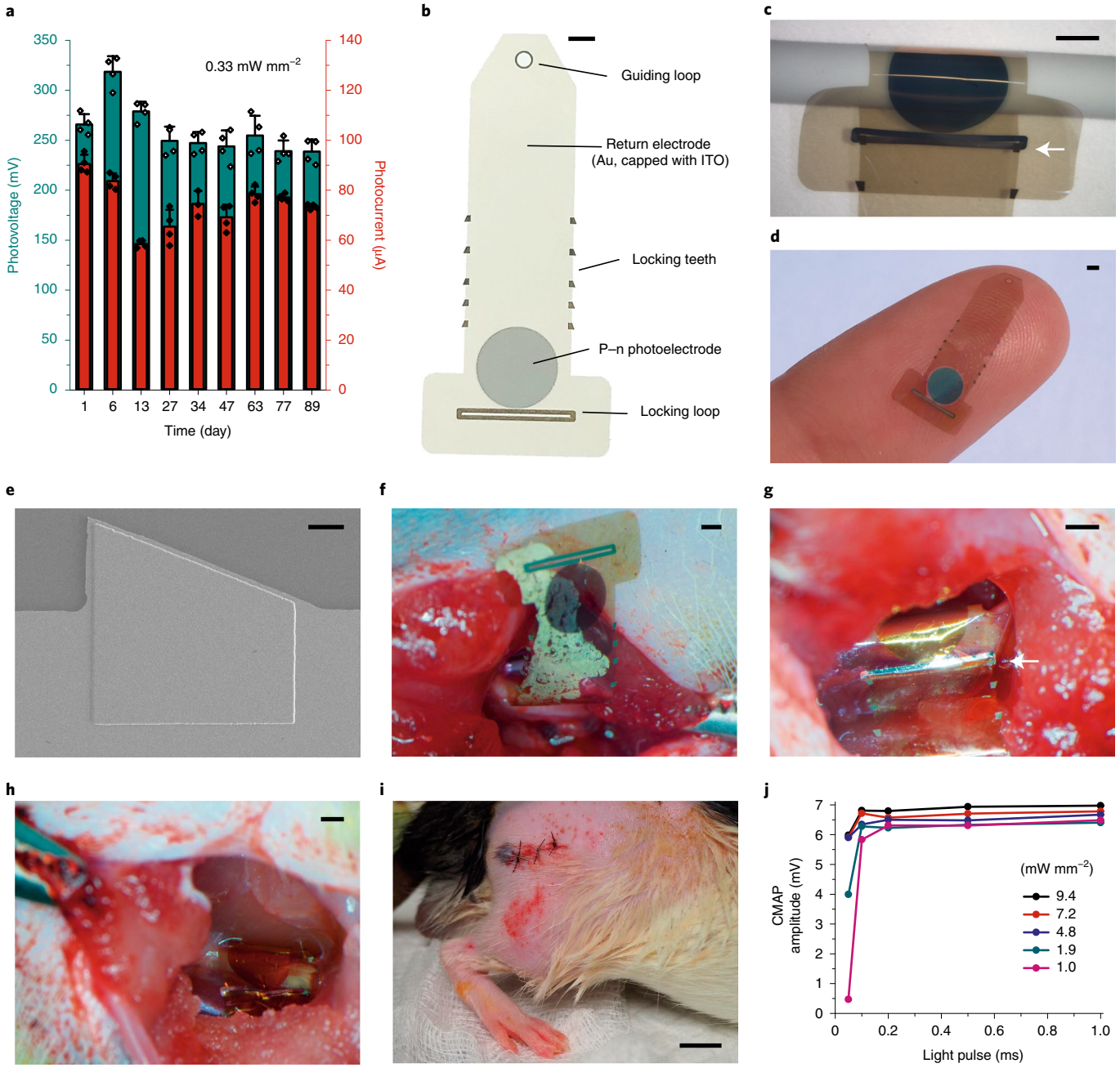

Fig. 4 | Self-fixating OEPCs are mechanically robust to intra-operative placement and chronic in vivo implantation. a, Verification of in vitro stability. The photovoltage and photocurrent were recorded periodically for devices subjected to accelerated aging conditions in 0.1 M KCl solution at 42 °C with light pulsing stress totalling 14 million charge/discharge cycles over 89 days ($n = 4$, average ± s.d.). **b**,**c**, Schematic (**b**) and photograph (**c**) of the zip-tie CIP device with labelled components (**b**) and when wrapped and locked around a nerve phantom (1.4-mm-diameter cylinder) (**c**). The white arrow indicates the locking tooth. Scale bars, 1 mm. **d**, Photograph of the conformable, ultralight and biocompatible CIP final design. Scale bar, 1 mm. **e**, Scanning electron microscopy image of the parylene-encapsulated aluminium tooth. Scale bar, 40 μm. **f**, CIP implantation was initiated by inserting the end of the ribbon behind the nerve and tucking it below the nerve. Scale bar, 1 mm. **g**, The p–n pixel was positioned adjacent to the external facing surface of the nerve, and the end of the ribbon was pulled through the loop to lock the ratchet teeth against the loop edges (white arrow). Scale bar, 1 mm. **h**, CIP device closed around the sciatic nerve. Scale bar, 1 mm. **i**, Sutured incision after CIP implantation was complete. Scale bar, 1 cm. **j**, Relationship between light intensity and pulse time (660-nm diode) and the CMAP amplitude for the implanted CIP device before incision closure.

O_2-reactive ion etching (Methods). ITO was used to protect the Au of the return electrode, and the Au without ITO capping remained the contact metal to the p–n layers. To predict the in vivo stability and functionality of the CIP devices, we conducted accelerated aging/stressing tests by immersing devices in 0.1 M KCl solution at 42 °C, and illuminating them with constant light pulses (2 Hz) delivered through a high-density LED array. Devices were periodically removed and the photovoltage and photocurrent were registered using the previously described EPR technique. No devices failed and the photovoltage and current retained greater than 85% of their starting values over the course of 89 days of continuous stressing (corresponding to 14 million charge/discharge cycles; Fig. 4a). Thus,

the ITO modification of the OEPC gives promising indications of robustness. Because the L-sized OEPCs performed optimally at low light intensities in the acute experiments, this p–n pixel size was used for fabrication of the CIP devices.

To ensure conformable contact with neural tissue and prevent damage caused by tension or pressure, we had chosen, from the start, to use ultrathin parylene C substrates for the OEPC neural interfaces. Parylene C can maintain mechanical contact via capillary forces in the presence of water, but this contact was insufficient to immobilize the device on the nerve for long-term stable stimulation. We thus adapted a parylene zip-tie locking mechanism[66,67] that allowed the device to form a cuff around the nerve in a fixed position. One end of the parylene C substrate ribbon was narrowed and modified to contain a small guiding loop, and the other end was widened to contain a narrow locking loop (Fig. 4b–d). When the guiding loop ribbon was passed through the locking loop, locking 'teeth' along the lateral borders of the ribbon allowed for sizing of the cuff diameter and prevented slippage of the ribbon ends (Fig. 4c). This CIP remained fully conformable and was sized to accommodate the dimensions of the rat sciatic nerve accessible through a minimally invasive surgical incision. Evaporated 1.5-μm-thick Al (a relatively malleable metal), encapsulated with parylene C, reinforced the loops and teeth (Fig. 4e). These Al-stiffened teeth and loops provided mechanical robustness of the locking mechanism and enabled facile manipulation with surgical tools during the implantation procedure.

Implantation was performed by sliding the ribbon of the CIP behind the sciatic nerve (Fig. 4f) and pulling the guiding loop through the locking loop with fine forceps (Fig. 4g). Once advanced through the locking teeth, the excess parylene C ribbon was trimmed and the sciatic nerve resumed its anatomical position relative to the muscles of the hindlimb (Fig. 4h). This procedure was straightforward and required 5 min of surgical time, fulfilling a key criterion for the translation of such devices to practical applications[68]. The incision was then sutured, separating the CIP from the surface of the skin by ~10–15 mm of skin, subcutaneous tissue and muscle (Fig. 4i). Before closure of the incision, CMAPs evoked by the CIP devices had light intensity-dependent amplitude responses comparable to those of the acutely implanted OEPCs, confirming that the design modifications to enable chronic implantation had not adversely affected the functionality (Fig. 4j). It should be noted that the absolute amplitudes of the registered CMAPs are lower under the chronic implant conditions because we used on-skin electrodes rather than inserting microwires into the muscle tissue.

We implanted CIP devices into a cohort of six rats and monitored their functionality at regular intervals over the course of three months. To minimize animal discomfort, we recorded CMAPs through gel-based cutaneous electrodes (Fig. 5a). Light stimulation from outside the body (using a 638-nm diode laser with an ~2 × 2-mm^2 illumination spot, maximum of 700 mW, as shown in Fig. 1d–f) elicited robust and repeatable CMAPs in all rats, some of which were associated with large-amplitude muscular twitches (Fig. 5b and Supplementary Video 2).

CIP devices generated detectable CMAPs in all rats for 20 days, and at least half were functional for longer than 60 days (Fig. 5c). In two rats, devices remained functional at timepoints greater than 100 days post-operatively, and CMAPs were obtainable in both the anaesthetized and awake states (Fig. 5d,e). Furthermore, when the CIPs were functional, the latency of CMAP onset from application of the light stimulus was relatively constant for light stimuli of variable intensity and duration (Fig. 5f), indicating stable nerve conduction velocity at the values expected for the intact rat sciatic nerve[69]. We observed that CMAP amplitude was typically stable for a prolonged time period without decay, but could experience abrupt decrement (Fig. 5d, left to middle) that was associated with slightly increased CMAP latency (Supplementary Fig. 2). However, the CIP devices remained capable of eliciting CMAPs with amplitude and latency similar to those obtained shortly after implantation when the light intensity was increased by eliminating tissue attenuation (Fig. 5d, right, Supplementary Video 3 and Supplementary Fig. 2). Given these results, we hypothesize that the alteration in CMAP properties during the implantation period was related to the generation of a submaximal neural excitatory pulse due to decreased CIP stimulation performance (that is, device degradation) rather than compromise of the nerve[70]. Post-mortem explantation of the CIP devices revealed partial delamination of the organic p–n material from the parylene C substrate (Supplementary Fig. 3). Partial delamination will render that part of the device unable to photogenerate current, thereby reducing stimulation efficacy. This is a possible degradation pathway. This observation of device degradation is in contrast to the results of the accelerated ageing tests in vitro shown in Fig. 4a. These findings highlight the importance of performing chronic in vivo experimentation to subject devices to the full range of biochemical and mechanical stressors present in a freely moving organism.

The preserved conduction velocity values we observed during CIP implantation suggested that the device did not result in functionally relevant nerve damage. None of the rats demonstrated motor deficit at any time post implantation, as all implanted rats were capable of

Fig. 5 | OEPCs permit chronic, non-invasive in vivo sciatic nerve stimulation. a, Healed implanted area after post-surgical recovery with surface electrodes for EMG measurements attached. Scale bar, 1 cm. **b**, Photoinduced stimulation for 200–1,000 μs using a 700 mW diode laser induced observable muscular twitches (Supplementary Video 2). Scale bar, 1 cm. **c**, Survival curve demonstrating the persistence of detectable CMAPs over the implantation period for all rats ($n = 6$). **d**, Representative averaged CMAPs over 103 days of chronic implantation. The CMAP amplitude abruptly decreased by 77 days post operation (PO), but the device was revealed to be functional with increased light delivery, accomplished by opening the overlying tissue. The red dashes indicate light stimulation pulses. **e**, Representative photoinduced CMAPs recorded in an awake rat. **f**, Stable average latency between a light pulse and the CMAP peak over the initial implantation period for the three rats with devices remaining functional for more than 60 days. **g**, Sciatic nerve implanted with a CIP device (69 days PO). Scale bar, 3 mm. **h**, Implanted sciatic nerve after 103 days PO (Imp.) did not show gross pathological changes as compared to the non-implanted contralateral sciatic nerve (Cntr.). The white dashed box shows the area where the CIP was implanted. Scale bar, 1 mm. **i**, Representative images of neurofilament and GFAP immunofluorescence (scale bar, 20 μm) of transverse sections from OEPC-implanted and sham sciatic nerves (collected 49–69 days PO). Insets show higher-magnification images (scale bar, 10 μm). **j**,**k**, Quantification of the number of immunopositive regions of interest (ROIs) per area, normalized to the respective sham samples value, for neurofilament (**j**, $n = 21$ sham nerves and $n = 25$ implanted sciatic nerves, three rats; $P = 0.64$) and GFAP (**k**, $n = 25$ sham nerves and $n = 26$ implanted nerves, three rats; two-sided t-test, $P = 0.63$). NS, not significant. **l**, All rats demonstrated similar hindlimb foot placement accuracy on the horizontal ladder task with sham and OEPC-implanted limbs (22–28 days PO, $n = 97$, 52, 135 and 132 steps for four rats). **m**, Hindlimb placement score on the horizontal ladder task averaged between trials for control ($n = 14$ trials, three rats) and sham/OEPC-implanted ($n = 19$ trials, four rats) groups (analysis of variance (ANOVA), Bonferroni post hoc test; control, $P = 1$; implanted, $P = 0.69$; control versus implanted $P = 0.72$). **n**, von Frey testing revealed that OEPC-implanted limbs did not exhibit a consistently different threshold for paw withdrawal (22–34 days PO, $n = 6$, 7, 5 and 5 and trials for four rats). **o**, The 50% threshold withdrawal response as calculated from von Frey testing for hindlimbs of control ($n = 18$ trials, three rats) and sham/OEPC-implanted ($n = 23$ trials, four rats) groups; different colours represent data from individual rats (ANOVA, Bonferroni post hoc test; control/implanted/control versus implanted, $P = 1$). All error bars indicate ±s.e.m.

running, standing on hindlimbs and climbing. To further assess this notion, we performed quantitative behavioural testing in an additional cohort of rats ($n=7$). Four rats underwent CIP implantation on one sciatic nerve and a sham surgical procedure on the contralateral limb. An additional three rats did not undergo any procedure and served as controls. Functional motor control was evaluated using a horizontal ladder task[71], with each hindlimb foot placement scored across experimental and control rats (Supplementary Video 4). We found no significant difference in the accuracy of hindlimb placement between CIP-implanted and CIP-non-implanted hindlimbs in experimental rats (Fig. 5l,m). Furthermore, comparison to the control cohort revealed no significant difference in task performance,

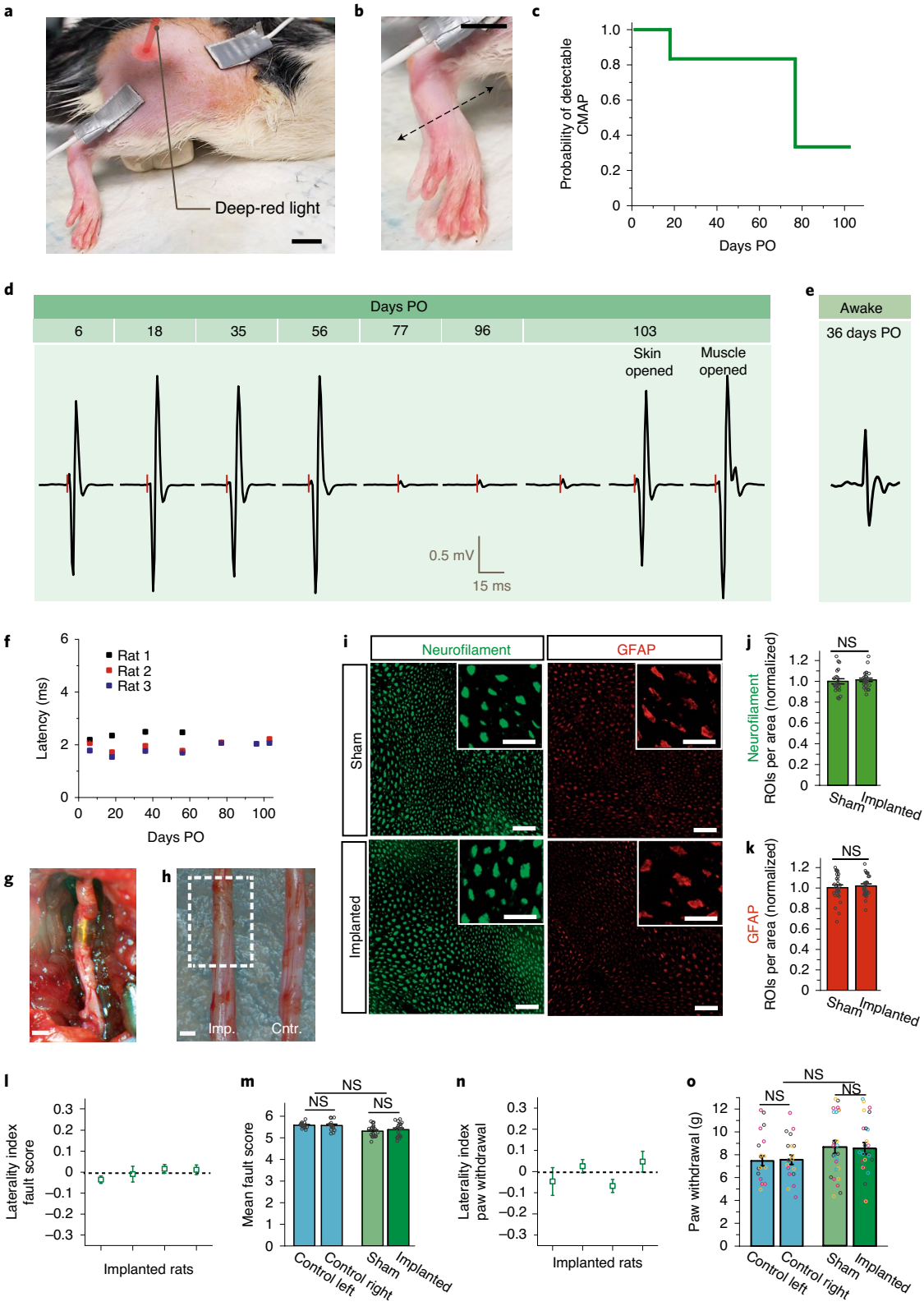

suggesting that CIP-implanted rats could not be distinguished from naïve animals in regard to motor function (Fig. 5m). We also evaluated this cohort for indicators of CIP-related neuropathy using the von Frey test. The threshold for paw withdrawal was determined as per established protocols[72]. We found that the paw innervated by the CIP-implanted nerve did not have a consistently different threshold for paw withdrawal across rats (Fig. 5n). There was also no significant difference in paw withdrawal threshold between the experimental and control rats (Fig. 5o). These results indicate that CIP implantation does not result in neuropathy.

Furthermore, we did not observe gross pathological differences between CIP-implanted sciatic nerves compared with sham surgical control nerves, suggesting that the conformable nature of the device prevented structural injury (Fig. 5g,h). Furthermore, there were no statistically significant different expression levels of neurofilament or glial fibrillary acidic protein, GFAP, between CIP-implanted nerves and sham controls (Fig. 5i–k). Together, our functional, behavioural and histological results support the preserved functionality of peripheral nerves chronically implanted with CIP devices.

Discussion

We have shown that ultrathin organic photocapacitors can be microfabricated into conformable devices that generate sufficient electrical charge to modulate neural tissue in vivo. Device-mediated neuromodulation is accomplished via tissue-penetrating deep-red light. Chronically implanted photocapacitors exhibit physiologic stability and functional stimulation of a peripheral nerve over months in a freely moving animal and do not incur motor deficit. In contrast to many other wireless neuromodulation devices, such as electromagnetic induction or ultrasound-based transducers, photocapacitors are microfabricated in a thin-film configuration, resulting in a minimally invasive interface with tissue.

Photocapacitors offer several advantages compared to other stimulation modalities. Conventional electrical stimulation is accomplished by wired leads connected to an implanted power source, a configuration that is a common cause of device complications[73]. We show that photocapacitors are capable of chronic electrical stimulation by directly converting light impulses into charge-balanced biphasic electrical signals, which is considered favourable for safe long-term stimulation[57]. Furthermore, the charge generated, and thus the neural response elicited, are directly related to the strength and duration of the light pulse. These features enable precise temporal and amplitude control of stimulation patterns. We have detailed how materials can be tailored to yield an ultrathin stimulator. First, robust and stable transparent conductors were optimized based on Au and ITO bilayers, which were engineered to stick reliably to the biocompatible polymer parylene C. Second, p–n stimulation pixels were designed to efficiently deliver stimulation currents while keeping the absorbing layers with a total thickness of 60 nm. Our work demonstrates that a conductor/semiconductor device layer combination with such low thickness can provide robust photovoltaic stimulation. Because photocapacitors are microfabricated, they are inherently customizable. The size, configuration and location of p–n junctions can be modified within a variable shape and size of ribbon substrate, permitting application to nerves of different diameters, as well as other types of neural tissue. Our flexible locking mechanism minimizes the risk of tissue damage while maintaining a steady device position in vivo. The combination of this fixing mechanism with the concentric arrangement of the charge-generating p–n pixel and the return electrode allows all the current to be directed into the nerve. In addition, no power source apart from the light pulse is necessary to operate the device, eliminating risks associated with implanted power hardware[74]. Photovoltaics based on the same active components as used in CIPs could also be used to non-invasively power other electrical components and enable information transmission via narrowband LEDs and photodiodes.

To facilitate the clinical translation of these photocapacitor devices, sustained performance should be demonstrated over prolonged time periods. The presented CIP devices functioned for months in a freely moving rodent and were not associated with detrimental behavioural or histological changes. There are three clear areas for optimization of the CIPs: improved device stability, greater efficiency and higher light sensitivity at longer wavelengths. Device longevity could be improved by encapsulation of the p–n pigment with a conductive layer that prevents exposure of the internal device layers to the electrolyte without decreasing the electrical performance. The second parameter to optimize is the light-to-charge efficiency of the devices, which would allow for operation in deeper tissues and increase the variety of targetable neural structures. Alternatively, it is possible to microfabricate conformable circuits that transmit electrical charge to deeper structures while maintaining the photoactive pigments closer to the external tissue interface for effective light activation. In terms of increasing the implantation depth for these technologies, much can be gained by tuning the stimulation wavelength. According to our MC model, a wavelength of 700 nm would be optimal in terms of transmission and would nearly double the possible implantation depth (Supplementary Fig. 4). On the other hand, tuning photocapacitor devices to respond even further to the red (800–900 nm) could also be advantageous for the comfort of human subjects, as at these wavelengths tissue transparency is sufficient for device operation, but human vision is no longer sensitive[39].

Electrical neurostimulation is employed not only to assay neural function in experimental paradigms[75], but is an efficacious and well-tolerated therapy for multiple neurologic disorders, from chronic pain to epilepsy[76]. CIPs can facilitate the testing of such neuromodulatory protocols in small-animal models by minimizing device footprint and allowing for full device implantation without any tissue-traversing elements, features that have been demonstrated to improve experimental outcomes[77,78]. The unique features of CIPs may also advance the potential for the translation of bioelectronic devices that require safe long-term neurostimulation to treat pain and to enable motor rehabilitation in humans.

Methods

OEPC device fabrication. H_2Pc (phthalocyanine, Alfa Aesar) and PTCDI (*N*,*N*′-dimethyl-3,4,9,10-perylenetetracarboxylic diimide, BASF) were first purified by threefold temperature-gradient sublimation. Four-inch soda-lime glass wafers (University Wafer, 550-µm-thick) were cleaned in a circulating 2% solution of Hellmanex III detergent heated to 50 °C for 30 min followed by a high-pressure rinse with acetone and deionized (DI) water. The wafers were then treated with O_2 plasma (Diener Electronic, 200 W, 20 min). Immediately afterwards, a 5-µm-thick parylene C layer was deposited by chemical vapour deposition (Diener Electronic). The parylene C was then patterned by lithography and etching to produce 4×15 mm² ribbons as follows. An Al reactive ion etching (RIE) hard mask was deposited through a stainless-steel shadow mask onto the parylene C wafer. The 80-nm layer of Al was evaporated in a physical vapor deposition (PVD) chamber in a vacuum of $<2\times10^{-6}$ torr at a rate of 5–15 Å s^{-1}. Parylene C was removed by RIE (200 W, O_2 100 s.c.c.m.). Finally, the Al mask was etched using a commercial wet-etch solution. The parylene surface was then activated with O_2 plasma (50 W, 2 min), followed by vapour-phase treatment with 3-(mercaptopropyl) trimethoxysilane (MPTMS) by placing the samples in an MPTMS-vapour saturated chamber heated to 90 °C for 1 h. MPTMS treatment enhanced the adhesion of Au to the parylene C substrate. Next, a 10-nm-thick film of Au was thermally evaporated over the whole wafer in a vacuum of $<2\times10^{-6}$ torr at a rate of 3–5 Å s^{-1}. The organic pigment p–n pixels were formed by thermal evaporation through a shadow mask at a base pressure of $<2\times10^{-6}$ torr at a rate of 0.1–0.5 nm s^{-1}. The 30 nm of p-type H_2Pc and 30 nm of n-type PTCDI were successively deposited, resulting in 60-nm total thickness of the organic layers (p–n). It should be noted that efforts were made to produce semi-transparent contacts from other materials, such as ITO. However, due to poor adhesion to the parylene substrate, approaches with ITO alone proved unsuccessful. Photothermal control samples were fabricated in the same way, except that, instead of the p–n layer, a 60-nm layer of indigo was thermally evaporated using the same conditions.

Optical tissue penetration modelling. MC light propagation simulation was conducted using CUDAMCML software[51], a graphics processing unit–accelerated

version of the well-established MCML software[50]. The tissue model consisted of three layers, a 1-mm layer of skin followed by 3 mm of subcutaneous adipose tissue and a 50-mm-thick layer of muscle. Rat-tissue optical parameters for all the wavelengths were taken from ref. [52]. Light penetration was evaluated on a 0.1-mm vertical and radial mesh. Five billion photons were used for each run of the simulation. The output files were convolved using CONV software (part of the MCML distribution), assuming a 2-mm-diameter (full-width at half-maximum) Gaussian light beam normalized to 700 mW of total power.

Photoelectrochemical characterization. Measurements of the photovoltage and charging current of the OEPC devices were performed according to previously described methods[46]. Briefly, the backside Au of the OEPC was contacted with a probe electrode connected to the positive terminal of an oscilloscope. Meanwhile, the negative terminal was connected to an Ag/AgCl electrode in 0.1 M KCl electrolyte, making contact to the top of the organic layer of the OEPC device. The droplet contact area was 0.126 cm^2. Pulsed illumination was provided by a 638-nm laser diode or a 660-nm high-power LED at various light intensities. The light intensity was verified using a calibrated Thorlabs Si p–i–n diode (Thorlabs SM1PD1B). The transient voltage change (V_T) was measured when the OEPC device was immersed in 0.1 M KCl, using a GeneClamp 500B amplifier (Axon Instruments) and a Digidata 1440A converter (Molecular Devices), as described previously[46]. It should be noted that the Ag/AgCl electrodes used in EPR measurements were illuminated and, at the wavelengths of light used (638–660 nm), we did not observe any signal, artefact or baseline shift related to illumination of the Ag/AgCl counterelectrode. Overall, we have not found any effects of photosensitivity of Ag/AgCl to the wavelengths used in our work.

Acute sciatic nerve stimulation. All animal experiments were approved by the institutional Animal Care and Use Committee of Columbia University Irving Medical Center. The implantations were carried out in Long Evans rats (200–250 g at the time of implantation) that had been subjected to no previous experimentation. Animals were housed in pairs, in a regular 12-h/12-h light/dark cycle, and had access to food and water ad libitum.

Rats were anaesthetized using isoflurane (3% for induction and 1–2% for maintenance), vaporized by a tabletop rodent anaesthesia set-up (V3000PL, Parkland Scientific). The fur at the surgical site was removed using Nair cream. The site was disinfected and local analgesia was applied. A longitudinal incision (~1 cm) along the femoral axis was performed and the sciatic nerve was visualized. The connective tissue surrounding the nerve was minimally dissected to release and expose a longitudinal nerve section (~4 mm long). The OEPC devices were wrapped around the nerve, facing the p–n pixel to the nerve surface, and fixed through adhesion of the parylene ribbon ends via capillary forces. Three p–n pixel diameter sizes (1, 1.4 and 3 mm) were tested. Tungsten microwires (diameter of 50 µm) were placed in the biceps femoris and plantar muscles, each providing a separate recording channel referenced to a microwire in the paraspinal subcutaneous tissue. CMAPs were recorded using a custom-designed board based on an AD8237 differential amplifier (Analog Devices) chip and an RHD2000 board (C3100, Intan Technologies) for digitization. Illumination was provided by a 660-nm high-power LED (M660L4, ThorLabs) with a collimator lens (SM2F32-B, ThorLabs) controlled by a ThorLabs DC2200 high-power LED driver. A minimum of 25 light pulses (with 3 s between) were used for each light intensity/duration condition tested. The CMAP amplitudes (maximal negative peak to maximal positive peak) were collected and averaged, using a customized Python code. Light intensity was verified with a Thorlabs SM1PD1B Si p–i–n diode. At the conclusion of the intra-operative recording session, the rats were euthanized. Five rats were used for acute sciatic nerve experiments that aimed to characterize the performance of OEPC devices regarding p–n pixel size, light intensity and light pulse duration.

Chronically implantable device fabrication. Clean 4-inch wafers were coated with 2.2 µm of parylene C. The surface was then activated by an oxygen plasma treatment (50 W, 120 s) followed by PVD of a 1.5–2-µm-thick layer of aluminium (vacuum of $<1\times10^{-5}$ torr, 20–30 nm s^{-1}) acting as a mechanical support for the locking mechanism structures. S1818 photoresist was spin-coated on the substrates, exposed with an MA6/BA6 Süss mask aligner and developed in MF-319. The Al layer was patterned using a commercial acidic etchant. The resist was stripped in acetone, followed by isopropanol and DI water. Propylene carbonate was then spin-coated on the wafers at 2,000 r.p.m. and baked at 60 °C for 30 s to act as an adhesion promoter[79] for the next 2.2-µm-thick encapsulating layer of parylene C. The surface was then exposed to oxygen plasma (50 W, 120 s) and vapour-treated with MPTMS in a closed chamber at 90 °C for 1 h. The wafers were washed with acetone, isopropanol and DI water. Next, 10 nm of gold and 30 nm of ITO were sputtered onto the substrates. The sputtering target was In_2O_3/SnO_2 90/10 wt%, 99.99% pure (Lesker). Gold was deposited at 100 W, 3.4 mTorr, 100% Ar, d.c. and ITO at 32 W, 4.5 mTorr, 97% Ar, 3% O_2, RF. The outline of the implants was patterned using S1818 photoresist, MF-319 developer, ITO etchant (concentrated HCl), Au etchant (KI/I_2) and finally by RIE (200 W, O_2 100 s.c.c.m.). The wafer was washed in acetone, isopropanol and DI water. A thin layer of 2% Micro90 cleaning agent was spin-coated at 1,000 r.p.m. to act as an anti-adhesive layer before the next 2.2-µm-thick sacrificial layer of parylene C. The openings for the photopixels were patterned by AZ 10XT resist, AZ developer and RIE (200 W, O_2 100 s.c.c.m.). The wafers were sequentially washed with acetone, isopropanol and DI water. The protective layer of ITO was then etched with concentrated HCl for a few seconds, followed by a quick wash in DI water. Next, the organic pigments H_2Pc and PTCDI were evaporated from resistively heated crucibles at 1×10^{-6} torr at rates of 1–6 Å s^{-1} to produce a 30/30-nm p–n junction. Finally, the sacrificial parylene layer was peeled off to yield the patterned device. The wafer was rinsed with DI water and tested using the EPR set-up described above. In addition, control devices were subjected to an accelerated ageing and light-stressing test according to a method described previously[47].

Chronic implantation test on the sciatic nerve. Rats were anaesthetized and the sciatic nerve exposed as previously described for acute stimulation. The CIP ribbon was passed behind the exposed sciatic nerve and the end of the ribbon was inserted through the ribbon loop using forceps. The p–n pixel was placed facing the nerve surface, and the ribbon was pulled until the teeth passed through the ribbon loop, firmly closing the zip-tie mechanism. The ribbon was adjusted to fit snugly around the nerve without applying compressive force. The excess ribbon (~5 mm) was then cut. Sutures were used to close the incision. After the operative procedure was complete, anaesthesia was removed and the rats were allowed to recover from surgery. Triple antibiotic ointment and injectable analgesia were applied during the post-surgical recovery period.

The CMAP recording sessions were performed at 6, 18, 35, 56, 77, 96 and 103 days post-operatively. Rats were anaesthetized (3% isoflurane) and the implanted site was shaved to facilitate attachment of electromyography electrodes to the skin. Because multiple recording sessions were planned for each rat, we performed non-invasive CMAP monitoring to prevent ongoing disruption of muscle tissue. Gel electrodes (14×9 mm^2, Acuzone) were attached to the skin using Elefix conductive paste (Nihon Kohden). Electrodes were placed on the gastrocnemius and vastus lateralis (reference electrode) muscles, maintaining a consistent inter-electrode distance across sessions. Photostimulation was induced by a 638-nm laser diode with a maximum output power of 700–1,200 mW driven by a ThorLabs DC2200 high-power LED controller. A total of 250 light pulses (3-s interpulse interval) with intensity spanning 700 mW to 7 mW and duration from 1 ms to 0.05 ms were used. A maximum power of 700 mW was used for all experiments up to 103 days, then the higher range up to 1,200 mW was tested at this point to try to maximize the CMAP responses. The illumination point was ~2 cm from the recording electrodes. CMAP signals were recorded as during the acute stimulation sessions. Video recordings of muscular twitches were performed.

The motor performance of the rats was evaluated in the immediate post-operative period and tested on an open field maze with horizontal and vertical obstacles at 53–54 days post-operatively. Walking and running gaits, as well as ability to stand on hindlimbs and climb, were observed.

In the subset of rats that showed responses after 103 days post operation, CMAPs were also recorded after creating an incision over the implantation site and opening the skin. Photoinduced stimulation was then repeated with the above parameters after exposing the device to quantify device performance under maximal light intensity conditions.

At the end of the implantation period, the rats were euthanized, and the implanted sciatic nerve section was collected and dissected. The contralateral sciatic nerve anatomically corresponding to the implanted region was also collected for comparison. Gross pathological examination was performed for all collected nerve segments. A total of 10 rats were chronically implanted with CIP devices.

Horizontal ladder test. The horizontal ladder rung apparatus had movable metal rungs (3-mm diameter) inserted between clear plexiglass side walls, irregularly spaced at 2 or 4 cm. The rung position pattern was modified daily to prevent the animal from learning the pattern and compensating for possible motor impairments. The animals were trained to cross the ladder over several sessions before recording and scoring the foot placement. The sessions were recorded using an Olympus E-M10 MII camera, positioned to optimally visualize foot placement. The hindlimb foot placement accuracy was visually analysed, frame by frame, using a seven-category scale according to ref. [71], from 0 (total miss) to 6 (correct placement). The start and end of the ladder, as well as the steps before and after a gait interruption, were excluded from the analysis. Both groups—control rats (no surgery) and chronic OEPC-implanted rats (tested 22 to 28 days after the implantation)—were used for the study. The implanted rats were additionally subjected to a sham surgery in the contralateral sciatic nerve, which consisted of an equivalent incision in the biceps femoris muscle, dissection of tissue to visualize and mobilize the sciatic nerve, and suturing for closure. A quantitative comparison of both hindlimbs was performed by averaging all the scores from each hindlimb placement across sessions and calculating the laterality index to determine whether there were any differences between performance of sham and OEPC-implanted limbs:

$$\frac{\text{Mean sham score} - \text{mean implanted score}}{\text{Mean sham score} + \text{mean implanted score}}$$

The statistical significance was calculated by applying ANOVA with the Bonferroni post hoc test.

Von Frey test. Von Frey tests were carried out as per established guidelines in ref. [72]. The rats were individually placed in bottom-opened cages on a wire mesh platform to allow full access to the feet. After 30 min of accommodation, tactile allodynia was evaluated for both hindlimbs in the awake animals using von Frey hair filaments from 0.4 to 16 g (TouchTest kit NC12775-99, North Coast Medical). The filaments were placed perpendicular to the hindlimb plantar surface, avoiding the footpads, and a positive response was considered to be paw withdrawal or flinching. Filaments were tested when no ambulatory or grooming activities were observed, waiting several minutes between consecutive trials. The paw withdrawal 50% threshold response for both hindlimbs was measured using the up–down paradigm[72]. A group of rats subjected to previously described OEPC device implantation and contralateral sham surgeries (22–34 days post implantation) were tested, as well as a control group. The 50% threshold response was averaged between different sessions for each hindlimb and the laterality index was calculated as previously described. Statistical significance was calculated by applying ANOVA with Bonferroni post hoc test.

Immunohistochemistry. Rats were perfused with paraformaldehyde (PFA) 4% and both sciatic nerves were collected, dissected and post fixated in PFA 4% at 4 °C for 12 h. A nerve section immediately distal to the implanted device and the equivalent section for the contralateral non-implanted sciatic nerve were collected and placed in agar (10%) blocks. Several transverse sections were obtained using a Leica VT1000S vibratome. The sections were subsequently washed in 0.01 M PBS and incubated in blocking solution (donkey serum 10% and T-X100 0.3% in PBS, room temperature (r.t.), 90 min). The samples were incubated with primary antibody against neurofilament (BioLegend, 837904; 1:200) or against GFAP (Dako, Z0334; 1:300) in PBS with T-X100 0.3%, at r.t., overnight. Following several washes in PBS with T-X100 0.3%, the sections were incubated with the corresponding secondary antibody Alexa 488 or Alexa 594 (R37114 or A-21207, Invitrogen; 1:250 in PBS with T-X100 0.3%, r.t., 3 h). Finally, the samples were washed in PBS with T-X100 0.3%, incubated with 4′,6-diamidino-2-phenylindole (1:10,000 in PBS with T-X100 0.3%, r.t., 20 min), washed again in PBS and mounted (Fluoromount Mounting Medium, Millipore-Sigma, F4680). All other used reagents were obtained from Millipore-Sigma. Fluorescence images were obtained using an Echo Revolve or Zeiss LSM 800 microscope. The same acquisition parameters were used to obtain all the images for the same immunostaining of implanted and sham sciatic nerve samples. Echo Pro and ZEN 3.2 software were used for image acquisition and the obtained images were processed using ImageJ. The number of immune-positive regions of interest per area were measured and normalized to the respective sham samples values. Statistical significance was calculated using Student's *t*-test.

Reporting summary. Further information on research design is available in the Nature Research Reporting Summary linked to this Article.

Data availability

The main data supporting the results in this study are available within the paper and its Supplementary Information. All data generated in this study, including source data and the data used to make the figures, are available from figshare with the identifier https://doi.org/10.6084/m9.figshare.15015099. Source data are provided with this paper.

Received: 2 July 2020; Accepted: 28 July 2021;
Published online: 16 December 2021

References

1. Krames, E. S., Peckham, P. H. & Rezai, A. R. (eds) *Neuromodulation* (Academic, 2009); https://doi.org/10.1023/B:MYCO.0000003704.30293.b6
2. Carrara, S. & Iniewski, K. (eds) *Handbook of Bioelectronics* (Cambridge Univ. Press, 2015); https://doi.org/10.1017/CBO9781139629539
3. Jastrzebska-Perfect, P. et al. Translational neuroelectronics. *Adv. Funct. Mater.* **30**, 1909165 (2020).
4. Lozano, A. M. et al. Deep brain stimulation: current challenges and future directions. *Nat. Rev. Neurol.* **15**, 148–160 (2019).
5. Chuang, A. T., Margo, C. E. & Greenberg, P. B. Retinal implants: a systematic review. *Br. J. Ophthalmol.* **98**, 852–856 (2014).
6. Johnson, R. L. & Wilson, C. G. A review of vagus nerve stimulation as a therapeutic intervention. *J. Inflamm. Res.* **11**, 203–213 (2018).
7. Ben-Menachem, E., Revesz, D., Simon, B. J. & Silberstein, S. Surgically implanted and non-invasive vagus nerve stimulation: a review of efficacy, safety and tolerability. *Eur. J. Neurol.* **22**, 1260–1268 (2015).
8. Caravaca, A. S. et al. An effective method for acute vagus nerve stimulation in experimental inflammation. *Front. Neurosci.* **13**, 877 (2019).
9. Birmingham, K. et al. Bioelectronic medicines: a research roadmap. *Nat. Rev. Drug Discov.* **13**, 399–400 (2014).
10. Acarón Ledesma, H. et al. An atlas of nano-enabled neural interfaces. *Nat. Nanotechnol.* **14**, 645–657 (2019).
11. Tanabe, Y. et al. High-performance wireless powering for peripheral nerve neuromodulation systems. *PLoS ONE* **12**, e0186698 (2017).
12. Larson, C. E. & Meng, E. A review for the peripheral nerve interface designer. *J. Neurosci. Methods* **332**, 108523 (2020).
13. Thimot, J. & Shepard, K. L. Bioelectronic devices: wirelessly powered implants. *Nat. Biomed. Eng.* **1**, 0051 (2017).
14. Agrawal, D. R. et al. Conformal phased surfaces for wireless powering of bioelectronic microdevices. *Nat. Biomed. Eng.* **1**, 0043 (2017).
15. Lee, B. et al. An implantable peripheral nerve recording and stimulation system for experiments on freely moving animal subjects. *Sci. Rep.* **8**, 6115 (2018).
16. Hernandez-Reynoso, A. G. et al. Miniature electroparticle-cuff for wireless peripheral neuromodulation. *J. Neural Eng.* **16**, 046002 (2019).
17. Singer, A. B. et al. Magnetoelectric materials for miniature, wireless neural stimulation at therapeutic frequencies. *Neuron* **107**, 631–643 (2020).
18. Cotero, V. et al. Noninvasive sub-organ ultrasound stimulation for targeted neuromodulation. *Nat. Commun.* **10**, 952 (2019).
19. Piech, D. K. et al. A wireless millimetre-scale implantable neural stimulator with ultrasonically powered bidirectional communication. *Nat. Biomed. Eng.* **4**, 207–222 (2020).
20. Murakawa, K., Kobayashi, M., Nakamura, O. & Kawata, S. A wireless near-infrared energy system for medical implants. *IEEE Eng. Med. Biol.* **18**, 70–72 (1999).
21. Kim, J. et al. Active photonic wireless power transfer into live tissues. *Proc. Natl Acad. Sci. USA* **117**, 16856–16863 (2020).
22. Jacques, S. L. Optical properties of biological tissues: a review. *Phys. Med. Biol.* **58**, 5007–5008 (2013).
23. Song, K. et al. Subdermal flexible solar cell arrays for powering medical electronic implants. *Adv. Healthc. Mater.* **5**, 1572–1580 (2016).
24. Haeberlin, A. et al. The first batteryless, solar-powered cardiac pacemaker. *Hear. Rhythm* **12**, 1317–1323 (2015).
25. Abdo, A. et al. Floating light-activated microelectrical stimulators tested in the rat spinal cord. *J. Neural Eng.* **8**, 056012 (2011).
26. Yun, S. H. & Kwok, S. J. J. Light in diagnosis, therapy and surgery. *Nat. Biomed. Eng.* **1**, 0008 (2017).
27. Park, S. et al. Self-powered ultra-flexible electronics via nano-grating-patterned organic photovoltaics. *Nature* **561**, 516–521 (2018).
28. Jiang, Y. et al. Rational design of silicon structures for optically controlled multiscale biointerfaces. *Nat. Biomed. Eng.* **2**, 508–521 (2018).
29. Scanziani, M. & Häusser, M. Electrophysiology in the age of light. *Nature* **461**, 930–939 (2009).
30. Richter, C. P. & Tan, X. Photons and neurons. *Hear. Res.* **311**, 72–88 (2014).
31. Shapiro, M. G., Homma, K., Villarreal, S., Richter, C.-P. & Bezanilla, F. Infrared light excites cells by changing their electrical capacitance. *Nat. Commun.* **3**, 736 (2012).
32. Jiang, Y. et al. Heterogeneous silicon mesostructures for lipid-supported bioelectric interfaces. *Nat. Mater.* **15**, 1023–1030 (2016).
33. Jiang, Y. & Tian, B. Inorganic semiconductor biointerfaces. *Nat. Rev. Mater.* **3**, 473–490 (2018).
34. Jiang, Y. et al. Nongenetic optical neuromodulation with silicon-based materials. *Nat. Protoc.* **14**, 1339–1376 (2019).
35. Sytnyk, M. et al. Cellular interfaces with hydrogen-bonded organic semiconductor hierarchical nanocrystals. *Nat. Commun.* **8**, 91 (2017).
36. Martino, N. et al. Photothermal cellular stimulation in functional bio-polymer interfaces. *Sci. Rep.* **5**, 8911 (2015).
37. Wang, L. et al. Photovoltaic retinal prosthesis: implant fabrication and performance. *J. Neural Eng.* **9**, 046014 (2012).
38. Ferlauto, L. et al. Design and validation of a foldable and photovoltaic wide-field epiretinal prosthesis. *Nat. Commun.* **9**, 992 (2018).
39. Mathieson, K. et al. Photovoltaic retinal prosthesis with high pixel density. *Nat. Photon.* **6**, 391–397 (2012).
40. Prévot, P. H. et al. Behavioural responses to a photovoltaic subretinal prosthesis implanted in non-human primates. *Nat. Biomed. Eng.* **4**, 172–180 (2019).
41. Hopkins, J. et al. Photoactive organic substrates for cell stimulation: progress and perspectives. *Adv. Mater. Technol.* **4**, 1800744 (2019).
42. Di Maria, F., Lodola, F., Zucchetti, E., Benfenati, F. & Lanzani, G. The evolution of artificial light actuators in living systems: from planar to nanostructured interfaces. *Chem. Soc. Rev.* **47**, 4757–4780 (2018).
43. Sytnyk, M. et al. Hydrogen-bonded organic semiconductor micro- and nanocrystals: from colloidal syntheses to (opto-)electronic devices. *J. Am. Chem. Soc.* **136**, 16522–16532 (2014).
44. Hunger, K. Toxicology and toxicological testing of colorants. *Rev. Prog. Color. Relat. Top.* **35**, 76–89 (2005).
45. Rand, D. et al. Direct electrical neurostimulation with organic pigment photocapacitors. *Adv. Mater.* **30**, 1707292 (2018).
46. Jakešová, M. et al. Optoelectronic control of single cells using organic photocapacitors. *Sci. Adv.* **5**, eaav5265 (2019).
47. Ejneby, M. S. et al. Extracellular photovoltage clamp using conducting polymer-modified organic photocapacitors. *Adv. Mater. Technol.* **5**, 1900860 (2020).

48. Merletti, R. & Parker, P. J. (eds) *Electromyography Physiology, Engineering and Noninvasive Applications* (Wiley, 2004).
49. Fortin, J. B. & Lu, T.-M. *Chemical Vapor Polymerization, The Growth and Properties of Parylene* (Springer, 2004).
50. Jacques, S. L. & Wang, L. MCML – Monte Carlo modeling of light transport in tissues. *Comput. Methods Prog. Biomed.* **47**, 131–146 (1995).
51. Alerstam, E., Svensson, T. & Andersson-Engels, S. Parallel computing with graphics processing units for high-speed Monte Carlo simulation of photon migration. *J. Biomed. Opt.* **13**, 060504 (2008).
52. Bashkatov, A. N., Genina, E. A. & Tuchin, V. V. Optical properties of skin, subcutaneous and muscle tissues: a review. *J. Innov. Opt. Health Sci.* **4**, 9–38 (2011).
53. *American National Standard for Safe Use of Lasers* ANSI Z136 (Laser Institute of America, 2007).
54. Cogan, S. F. Neural stimulation and recording electrodes. *Annu. Rev. Biomed. Eng.* **10**, 275–309 (2008).
55. Boehler, C., Carli, S., Fadiga, L., Stieglitz, T. & Asplund, M. Tutorial: guidelines for standardized performance tests for electrodes intended for neural interfaces and bioelectronics. *Nat. Protoc.* **15**, 3557–3578 (2020).
56. Đerek, V., Rand, D., Migliaccio, L., Hanein, Y. & Głowacki, E. D. Untangling photofaradaic and photocapacitive effects in organic optoelectronic stimulation devices. *Front. Bioeng. Biotechnol.* **8**, 284 (2020).
57. Merrill, D. R., Bikson, M. & Jefferys, J. G. R. Electrical stimulation of excitable tissue: design of efficacious and safe protocols. *J. Neurosci. Methods* **141**, 171–198 (2005).
58. Harnack, D. et al. The effects of electrode material, charge density and stimulation duration on the safety of high-frequency stimulation of the subthalamic nucleus in rats. *J. Neurosci. Methods* **138**, 207–216 (2004).
59. Schoen, I. & Fromherz, P. Activation of Na^+ channels in cell membrane by capacitive stimulation with silicon chip. *Appl. Phys. Lett.* **87**, 193901–193903 (2005).
60. Seixas de Melo, J. et al. Photophysics of an indigo derivative (keto and leuco structures) with singular properties. *J. Phys. Chem. A* **110**, 13653–13661 (2006).
61. Jeppesen, C., Mortensen, N. A. & Kristensen, A. The effect of Ti and ITO adhesion layers on gold split-ring resonators. *Appl. Phys. Lett.* **97**, 2012–2015 (2010).
62. Benck, J. D., Pinaud, B. A., Gorlin, Y. & Jaramillo, T. F. Substrate selection for fundamental studies of electrocatalysts and photoelectrodes: inert potential windows in acidic, neutral and basic electrolyte. *PLoS ONE* **9**, e107942 (2014).
63. Matarese, B. et al. Investigation of the stability and biocompatibility of commonly used electrode materials in organic neuro-optoelectronics. In *Proc. 2015 IEEE 15th International Conference on Nanotechnology* (*IEEE-NANO*) 1539–1542 (IEEE, 2015).
64. Selvakumaran, J., Hughes, M. P., Ewins, D. J. & Richards, P. R. Biocompatibility studies of materials used for chronically implantable microelectrodes. In *Proc. 1st Annual International IEEE-EMBS Special Topic Conference on Microtechnologies in Medicine and Biology* 521–525 (IEEE, 2000); https://doi.org/10.1109/MMB.2000.893839
65. Ilic, B. & Craighead, H. G. Topographical patterning of chemically sensitive biological materials using a polymer-based dry lift off. *Biomed. Microdev.* **2**, 317–322 (2000).
66. Yu, H., Xiong, W., Zhang, H., Wang, W. & Li, Z. A cable-tie-type parylene cuff electrode for peripheral nerve interfaces. In *Proc. 2014 IEEE 27th International Conference on Micro Electro Mechanical Systems* (*MEMS*) 9–12 (IEEE, 2014); https://doi.org/10.1109/MEMSYS.2014.6765560
67. Cobo, A. M. et al. Parylene-based cuff electrode with integrated microfluidics for peripheral nerve recording, stimulation and drug delivery. *J. Microelectromech. Syst.* **28**, 36–49 (2019).
68. Günter, C., Delbeke, J. & Ortiz-Catalan, M. Safety of long-term electrical peripheral nerve stimulation: review of the state of the art. *J. Neuroeng. Rehabil.* **16**, 13 (2019).
69. Ayaz, M. et al. Sexual dependency of rat sciatic nerve fiber conduction velocity distributions. *Int. J. Neurosci.* **117**, 1537–1549 (2007).
70. Koo, Y. S., Cho, C. S. & Kim, B. J. Pitfalls in using electrophysiological studies to diagnose neuromuscular disorders. *J. Clin. Neurol.* **8**, 1–14 (2012).
71. Metz, G. A. & Whishaw, I. Q. The ladder rung walking task: a scoring system and its practical application. *J. Vis. Exp.* **28**, 1204 (2009).
72. Chaplan, S. R., Bach, F. W., Pogrel, J. W., Chung, J. M. & Yaksh, T. L. Quantitative assessment of tactile allodynia in the rat paw. *J. Neurosci. Methods* **53**, 55–63 (1994).
73. Cameron, T. Safety and efficacy of spinal cord stimulation for the treatment of chronic pain: a 20-year literature review. *J. Neurosurg.* **100**, 254–267 (2004).
74. Perryman, L. T. Spinal cord stimulation costs and complications can be reduced by wireless nanotechnology. A review of traditional equipment expenses compared to wireless stimulation. *Am. J. Anesth. Clin. Res.* **4**, 19–24 (2018).
75. Krook-Magnuson, E., Gelinas, J. N., Soltesz, I. & Buzsáki, G. Neuroelectronics and biooptics: closed-loop technologies in neurological disorders. *JAMA Neurol.* **72**, 823–829 (2015).
76. Edwards, C. A., Kouzani, A., Lee, K. H. & Ross, E. K. Neurostimulation devices for the treatment of neurologic disorders. *Mayo Clin. Proc.* **92**, 1427–1444 (2017).
77. Gutruf, P., Good, C. H. & Rogers, J. A. Perspective: implantable optical systems for neuroscience research in behaving animal models—current approaches and future directions. *APL Photon.* **3**, 120901 (2018).
78. Lu, L. et al. Wireless optoelectronic photometers for monitoring neuronal dynamics in the deep brain. *Proc. Natl Acad. Sci. USA* **115**, E1374–E1383 (2018).
79. Chang, J. H.-C., Lu, B. & Tai, Y.-C. Adhesion-enhancing surface treatments for parylene deposition. In *Proc. 2011 16th International Solid-State Sensors, Actuators and Microsystems Conference* 390–393 (IEEE, 2011).

Acknowledgements

This project has received funding from the European Research Council (ERC) under the European Union's Horizon 2020 research and innovation programme (grant agreement no. 949191, E.D.G.). We acknowledge financial support from the Knut and Alice Wallenberg Foundation within the framework of the Wallenberg Centre for Molecular Medicine at Linköping University (E.D.G.), the Swedish Research Council (Vetenskapsrådet, 2018-04505, E.D.G.) and the Swedish Foundation for Strategic Research (E.D.G. and M.B.). This work was also supported by Columbia University, School of Engineering and Applied Science, as well as Columbia University Medical Center, Department of Neurology and Institute for Genomic Medicine. We acknowledge CzechNanoLab Research Infrastructure, supported by MEYS CR (LM2018110). This work has been supported by the Croatian Science Foundation under project UIP-2019-04-1753 (V.Đ.). V.Đ. acknowledges the support of project CeNIKS, co-financed by the Croatian Government and the European Union through the European Regional Development Fund – Competitiveness and Cohesion Operational Programme (grant no. KK.01.1.1.02.0013), and the QuantiXLie Center of Excellence, a project co-financed by the Croatian Government and European Union through the European Regional Development Fund – the Competitiveness and Cohesion Operational Programme (grant no. KK.01.1.1.01.0004). Financial support by the Center of Excellence for Advanced Materials and Sensors, Croatia, is gratefully acknowledged. We also thank H. Khodagholy for the design and fabrication of the horizontal ladder apparatus.

Author contributions

M.S.E., M.J. and L.M. carried out the photoelectrochemical characterizations. M.S.E., M.J., V.Đ., D.K. and J.N.G. performed acute experiments and analysed data. L.M. fabricated the devices for the acute experiments. M.J. fabricated the devices for the chronic experiments. V.Đ. wrote programs for data acquisition, processing and MC modelling. I.S. performed calculations with finite-element models. Z.Z. designed and developed the electrophysiological acquisition hardware. J.J.F., D.K. and J.N.G. performed the rodent surgeries. Chronic data were collected and analysed by M.J., J.J.F., Z.Z., J.N.G. and E.D.G. J.J.F. and M.S.E. performed the rat behavioural testing. J.J.F. conducted immunohistochemistry experiments. The project was led and supervised by M.B., D.K., V.Đ., J.N.G. and E.D.G. The manuscript was written with input from all co-authors.

Competing interests

The authors declare no competing interests.

Additional information

Supplementary information The online version contains supplementary material available at https://doi.org/10.1038/s41551-021-00817-7.

Correspondence and requests for materials should be addressed to Vedran Đerek, Jennifer N. Gelinas or Eric Daniel Głowacki.

Peer review information *Nature Biomedical Engineering* thanks Gregoire Courtine, John Ho and Bozhi Tian for their contribution to the peer review of this work.

nature research

Corresponding author(s): Vedran Derek, Jennifer Gelinas and Eric Glowacki

Last updated by author(s): Jul 19, 2021

Reporting Summary

Nature Research wishes to improve the reproducibility of the work that we publish. This form provides structure for consistency and transparency in reporting. For further information on Nature Research policies, see our Editorial Policies and the Editorial Policy Checklist.

Statistics

For all statistical analyses, confirm that the following items are present in the figure legend, table legend, main text, or Methods section.

n/a	Confirmed	
☐	☒	The exact sample size (*n*) for each experimental group/condition, given as a discrete number and unit of measurement
☐	☒	A statement on whether measurements were taken from distinct samples or whether the same sample was measured repeatedly
☐	☒	The statistical test(s) used AND whether they are one- or two-sided *Only common tests should be described solely by name; describe more complex techniques in the Methods section.*
☒	☐	A description of all covariates tested
☒	☐	A description of any assumptions or corrections, such as tests of normality and adjustment for multiple comparisons
☐	☒	A full description of the statistical parameters including central tendency (e.g. means) or other basic estimates (e.g. regression coefficient) AND variation (e.g. standard deviation) or associated estimates of uncertainty (e.g. confidence intervals)
☐	☒	For null hypothesis testing, the test statistic (e.g. *F*, *t*, *r*) with confidence intervals, effect sizes, degrees of freedom and *P* value noted *Give P values as exact values whenever suitable.*
☐	☒	For Bayesian analysis, information on the choice of priors and Markov chain Monte Carlo settings
☒	☐	For hierarchical and complex designs, identification of the appropriate level for tests and full reporting of outcomes
☒	☐	Estimates of effect sizes (e.g. Cohen's *d*, Pearson's *r*), indicating how they were calculated

Our web collection on statistics for biologists contains articles on many of the points above.

Software and code

Policy information about availability of computer code

Data collection	Intan RHX 3.0.1 (Open source aquisition software for the RHD2000 Intan system).
Data analysis	Origin 8.5, GraphPad Prism 7.05, Matlab.

For manuscripts utilizing custom algorithms or software that are central to the research but not yet described in published literature, software must be made available to editors and reviewers. We strongly encourage code deposition in a community repository (e.g. GitHub). See the Nature Research guidelines for submitting code & software for further information.

Data

Policy information about availability of data

All manuscripts must include a data availability statement. This statement should provide the following information, where applicable:

- Accession codes, unique identifiers, or web links for publicly available datasets
- A list of figures that have associated raw data
- A description of any restrictions on data availability

The main data supporting the results in this study are available within the paper and its Supplementary Information. All data generated in this study, including source data and the data used to make the figures, are available from figshare with the identifier https://doi.org/10.6084/m9.figshare.15015099.

Field-specific reporting

Please select the one below that is the best fit for your research. If you are not sure, read the appropriate sections before making your selection.

☒ Life sciences ☐ Behavioural & social sciences ☐ Ecological, evolutionary & environmental sciences

For a reference copy of the document with all sections, see nature.com/documents/nr-reporting-summary-flat.pdf

Life sciences study design

All studies must disclose on these points even when the disclosure is negative.

Sample size	Acute validation of wireless neurostimulation was carried out in five rats, with EMG data collection being done in the same way in each animal. Owing to the high reproducibility seen, the use of more animals was judged not to be warranted. Sample-size requirements were estimated on the basis of the relevant literature and on an acceptable number of replicates for in vivo animal experimentation on peripheral nerves. The high reproducibility of the data and the low variability of the responses supported this approach.
Data exclusions	While conducting acute stimulation experiments analysing EMG amplitude as a function of light power and pulse duration (Figure 2g,h), it was challenging to select a recording gain value that was appropriate in order to capture the whole dynamic range of EMG amplitude. It was sometimes the case that for the highest values of light power and pulse duration, the EMG signal was saturated (that is, 'clipped'). Scans with clipped EMG values were excluded. With a judicious selection of amplifier gain, this problem could be avoided; nevertheless, it was difficult to establish during the experiment whether the final data points may be clipped (this was apparent only after plotting the data).
Replication	Acute photostimulation of the sciatic nerve was characterized in five rats, and subsequently chronic stimulation was conducted in six additional rats. Therefore, the efficacy of stimulation was validated in multiple animals and over multiple experimental sessions. All animals implanted with a photocapacitor device demonstrated photostimulation, without exception.
Randomization	This was not applicable to the study, as comparisons of effects between populations were not a part of it. All rats used for control/sham/ experimental implantation were of the same type and were handled the same way.
Blinding	The experimental outcome, in the form of EMG recordings, cannot be influenced by an experimenter bias. The detection and characterization of CMAPs were performed with the analyser being blind to the stimulation protocol employed, with blinding removed for group comparisons. We therefore judged that no special blinding measures were necessary. The stimulation and recording procedures were identical for sham animals and for animals implanted with a photocapacitor. There is not a reasonable way in which an experimenter can influence the EMG signal, especially because in control/sham animals there was no observable stimulation.

Reporting for specific materials, systems and methods

We require information from authors about some types of materials, experimental systems and methods used in many studies. Here, indicate whether each material, system or method listed is relevant to your study. If you are not sure if a list item applies to your research, read the appropriate section before selecting a response.

Materials & experimental systems

n/a	Involved in the study
☒	☐ Antibodies
☒	☐ Eukaryotic cell lines
☒	☐ Palaeontology and archaeology
☐	☒ Animals and other organisms
☒	☐ Human research participants
☒	☐ Clinical data
☒	☐ Dual use research of concern

Methods

n/a	Involved in the study
☒	☐ ChIP-seq
☒	☐ Flow cytometry
☒	☐ MRI-based neuroimaging

Animals and other organisms

Policy information about studies involving animals; ARRIVE guidelines recommended for reporting animal research

Laboratory animals	Long Evans rats, male, 200–250g at the time of implantation.
Wild animals	The study did not involve wild animals.
Field-collected samples	The study did not involve samples collected from the field.

Ethics oversight	All animal experiments were approved by the institutional Animal Care and Use Committee of Columbia University Irving Medical Center.

Note that full information on the approval of the study protocol must also be provided in the manuscript.